New levels of high angular resolution EBSD performance via inverse compositional Gauss-Newton digital image correlation

T.J. Ruggles[a,*], G.F. Bomarito[b], R.L. Qiu[c], J.D. Hochalter[b]

[a]*National Institute of Aerospace, 100 Exploration Way, Hampton, VA 23666, USA*
[b]*National Air and Space Administration, Hampton, VA 23666*
[c]*Roanoke Valley Governor's School for Science and Technology, Roanoke, VA 24015*

Abstract

Conventional high angular resolution electron backscatter diffraction (HREBSD) uses cross-correlation to track features between diffraction patterns, which are then related to the relative elastic strain and misorientation between the diffracting volumes of material. This paper adapts inverse compositional Gauss Newton (ICGN) digital image correlation (DIC) to be compatible with HREBSD. ICGN works by efficiently tracking not just the shift in features, but also the change in their shape. Modeling a shape change as well as a shift results in greater accuracy. This method, ICGN HREBSD, is applied to a simulated data set, and its performance is compared to conventional cross-correlation HREBSD, and cross-correlation HREBSD with remapping. ICGN HREBSD is shown to have about half the strain error of the best cross-correlation method with a comparable computation time.

Keywords: HREBSD, DIC, Simulated EBSD patterns

1. Introduction

Electron backscatter diffraction (EBSD) is a material characterization technique where dynamic diffraction patterns are collected in a scanning electron microscope. Diffraction bands in these patterns are typically identified in commercial software via the Hough transform, and the pattern is subsequently indexed by comparing the relative angle of the bands. These methods have an accuracy of 0.1-0.5^{o} and potentially higher precision [1–3]. The spatial resolution is limited by the interaction volume of the electron beam with the sample, which has a size on the order of hundreds of nanometers [4]. For grain size distribution

and texture of engineering materials, this precision is adequate, but additional information can be extracted via high resolution EBSD methods, including more accurate orientations, dislocation content, elastic strain, stress, variations in the local lattice parameters, etc. This information can be used to develop high fidelity material models [5, 6].

High angular resolution electron backscatter diffraction (HREBSD) was first pioneered by Troost [7] and was fully implemented by Wilkinson, Meaden and Dingley [8, 9]. The method involves performing cross-correlation between a reference EBSD pattern and a test pattern over a number of regions of interest (ROIs). The shifts between ROIs are related by the geometry of diffraction to the relative elastic deformation gradient between the volumes of material from which the diffraction patterns originated. HREBSD provides more precision than conventional EBSD indexing, and also provides elastic strain data along with relative rotation. The theoretical precision of HREBSD, based on the typical pixel resolution of the cameras used to collect EBSD patterns and typical detector set-ups, is around 200 microstrain [9, 10]. Practical issues, such as low diffraction pattern quality [11–13], camera lens distortion [14], uncertainty in the precise location of the origin of the diffraction pattern [14–19] and large misorientation angles between patterns [10, 20] mean that considerably less precision is achieved in practice. The latter problem is addressed by pattern remapping, a method by which either the reference or the test pattern is warped to match the other as closely as possible, which improves the accuracy of cross-correlation.

Advanced methods from digital image correlation (DIC) may be applied to HREBSD to address the misorientation problem. HREBSD, at its core, is an image processing algorithm used to measure the relative deformation between images, making HREBSD a specialized instance of DIC [21–23]. HREBSD uses the simplest form of DIC, normalized cross-correlation, where the form of the deformation between regions of interest, referred to as the warping function, is assumed to be a pure shift (zero order polynomial). For higher accuracy, many DIC methods approximate the warping function as linear (first order) or quadratic (second order) polynomials [21, 22]. Neither warping function is appropriate for HREBSD. This is because a linear deformation in three space becomes a non-polynomial deformation when projected onto a two-dimensional surface. This paper presents a form of DIC where the warping function is specifically tailored to a deformed EBSD pattern projected onto the phosphor screen used to collect the pattern. The approach taken here is similar to the work of Vermeij and Hoefnagels [24], which was conducted independently.

Accommodating for the warping of an ROI is much more computationally intensive than normalized cross-correlation, which can be measured efficiently using Fourier transforms. It requires the solution of a computationally expensive non-linear optimization problem. To mitigate the computational expense of this problem, in this paper the inverse compositional Gauss-Newton (ICGN) method [25, 26] is used. ICGN is a gradient based optimization routine that only requires approximation of the Hessian once. The ICGN HREBSD method presented here will be compared to various implementations of cross-correlation HREBSD using a simulated data set: simple cross-correlation, cross-correlation with a remapping step and cross-correlation with iterative remapping. ICGN is shown to have around half the strain error of cross-correlation with iterative remapping. This improvement in strain resolution is essential when incorporating HREBSD data into high fidelity material models.

2. Background

Cross-correlation HREBSD is a method where the shifts between features of two patterns (referred to here as a reference pattern and a test pattern) are measured and then used to calculate their relative deformation gradient, $\mathbf{F}$. The features used to determine the shift, $\vec{q}$, are typically square ROIs on the patterns. The relationship between $\mathbf{F}$ and $\vec{q}$ is diagrammed in Figure 1. Simple cross-correlation is the fastest way to measure these shifts because they can be determined using discreet Fourier transforms. However, normalized cross-correlation is preferred as it prevents single bright spots or gradients from interfering with the shift calculation [27]. Instead, each ROI is put through a band pass filter to approximate normalized cross-correlation. Additionally, a window function is typically applied. Sub-pixelar resolution in the shift is obtained by using a simple fit on the cross-correlation peak; in this paper, a quadratic fit is used. Typically, each ROI of the reference pattern is cross-correlated with a comparable ROI in the test pattern, rather than the entire image, to save computation time. For better results, the location of the ROI on the test pattern may be offset by an integer pixel distance based on an estimate of the deformation from conventional EBSD indexing.

Once obtained, these shifts are related via the projection geometry to the deformation gradient. The relevant projection parameters include the location of the reference pattern's source relative to the phosphor screen used to collect the pattern, a.k.a. the pattern center ($\vec{P}$), the pattern center of the test pattern, (here

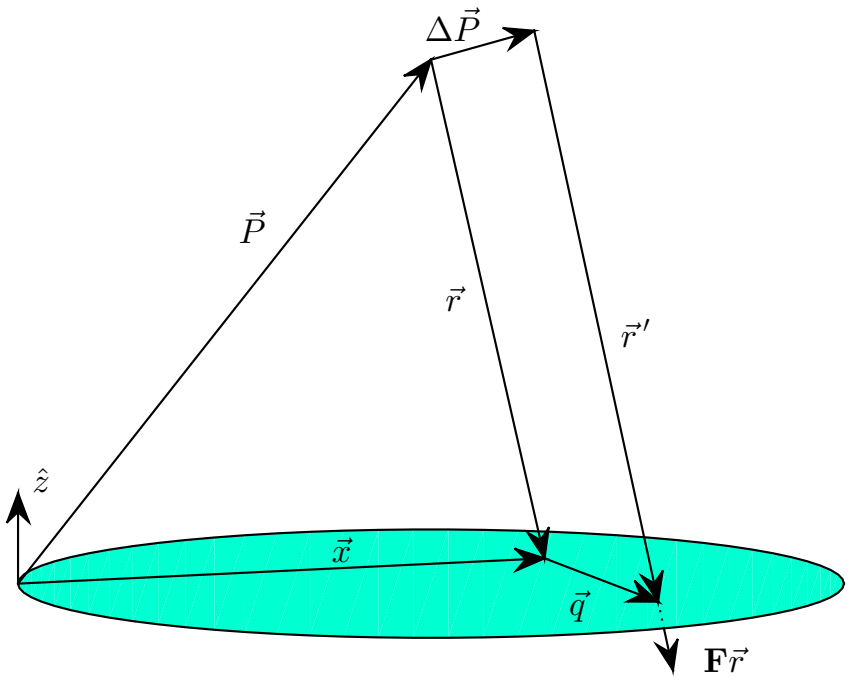

Figure 1: Illustration of the geometry of HREBSD relative to the phosphor screen (bottom).

represented as a deviation from the reference pattern center: $\vec{P}+\Delta\vec{P}$), and the location of the reference feature on the phosphor screen, $\vec{x}$. The vectors $\vec{r}$ and $\vec{r}'$ represent the vector from the reference pattern center to the feature on the reference pattern and the vector from the test pattern center to the corresponding feature on the test pattern, respectively. The unit vector $\hat{z}$ is normal to the phosphor screen. From Figure 1 the following relationships exist:

$$\vec{q} = \Delta\vec{P} + \vec{r}' - \vec{r} \tag{1}$$

$$\vec{r} = \vec{x} - \vec{P} \tag{2}$$

Next, it is assumed there is some deformation gradient, $\mathbf{F}$, that operates on $\vec{r}$. The deformed vector is parallel to $\vec{r}'$:

$$\mathbf{F}\vec{r} \parallel \vec{r}' \tag{3}$$

Because $\vec{r}'$ must end on the phosphor screen, its z-component must be equal and opposite of the z-component

of the pattern center of the deformed pattern, which allows $\vec{r}'$ to be expressed in terms of $\mathbf{F}$ as:

$$\vec{r}' = \mathbf{F}\vec{r}\frac{-(\vec{P}+\Delta\vec{P})\cdot\hat{z}}{\mathbf{F}\vec{r}\cdot\hat{z}} \tag{4}$$

Substitutions of Equation 4 into Equation 1 now gives us the relationship of the shifts between two patterns and the relative deformation gradient between them:

$$\vec{q} = \Delta\vec{P} + \mathbf{F}\vec{r}\frac{-(\vec{P}+\Delta\vec{P})\cdot\hat{z}}{\mathbf{F}\vec{r}\cdot\hat{z}} - \vec{r} \tag{5}$$

When the difference between the pattern centers of the reference and test patterns, $\Delta\vec{P}$, is assumed to be zero (the norm for most derivations of this relationship) and the substitution $-\vec{P}\cdot\hat{z} = \vec{r}\cdot\hat{z}$ is made, this relationship becomes:

$$\vec{q} = \mathbf{F}\vec{r}\frac{\vec{r}\cdot\hat{z}}{\mathbf{F}\vec{r}\cdot\hat{z}} - \vec{r} \tag{6}$$

which is much easier to rearrange and solve for the components of $\mathbf{F}$. By making the substitution $\beta = \mathbf{F} - \mathbf{I}$ (where $\mathbf{I}$ is the identity matrix) and expressing the problem term-wise, we get the following:

$$q_1 = \beta_{11}r_1 + \beta_{12}r_2 + \beta_{13}r_3 - \frac{1}{r_3}(q_1 + r_1)(\beta_{31}r_1 + \beta_{32}r_2 + \beta_{33}r_3) \tag{7}$$

$$q_2 = \beta_{21}r_1 + \beta_{22}r_2 + \beta_{23}r_3 - \frac{1}{r_3}(q_2 + r_2)(\beta_{31}r_1 + \beta_{32}r_2 + \beta_{33}r_3) \tag{8}$$

Note that Equations 1-6 are reference frame agnostic, but for the term-wise equations the coordinate frame of the phosphor screen is assumed, where q_3 and x_3 are zero. Aside from simplifying the component-wise expressions for these relationships, rotating into the the phosphor frame also naturally sequesters the linear and non-linear components of β into separate terms, making this an extremely convenient reference frame for HREBSD calculation [18].

Equations 7-8 represent the relationship between β and the shift of a single ROI: two equations with nine degrees of freedom corresponding to the components of β. Using Equations 7-8 from at least four non-co-linear ROIs allows us to recover eight degrees of freedom of β, but the assembled equations will never be full-rank because of the information lost during projection. The ninth degree of freedom is recovered

by adding an additional constraint, either the traction free constraint [10, 28] or enforcing the stress to be deviatoric [20]. In practice, anywhere from 20 to 200 overlapping ROIs are used and β is determined with a least-squares fit.

The difference in pattern center, $\Delta\vec{P}$, must be accounted for when it is known and non-zero. To this end, it is convenient to rearrange Equation 5 such that the right hand side is identical to the right hand side of Equation 6:

$$\vec{q}^{*} = \left(\vec{q} - \Delta\vec{P} + \vec{r}\right) \frac{\vec{P}\cdot\hat{z}}{\left(\vec{P} + \Delta\vec{P}\right)\cdot\hat{z}} - \vec{r} = \mathbf{F}\vec{r}\frac{\vec{r}\cdot\hat{z}}{\mathbf{F}\vec{r}\cdot\hat{z}} - \vec{r} \tag{9}$$

where $\vec{q}^{*}$ is the effective shift if the reference and test pattern centers were identical. Calculation of $\vec{q}^{*}$ makes Equations 7-8 valid regardless of a difference in pattern center.

There are several known limitations to the accuracy of cross-correlation HREBSD as described so far. The first is that HREBSD only determines the relative strains between patterns, but absolute strains are preferable. In the case of studying local plastic behavior, such as nano-indentation or when plasticity is limited to the area around a crack tip, finding a relatively strain-free reference pattern is fairly simple [29]. Alternatively, simulated, strain-free diffraction patterns of known orientation can be used as a reference [14, 19, 30–32]. The next major source of error is uncertainty in the location of the pattern center, which can be on the order of 500 μm when calibrated using iterative fitting methods. Using simulated patterns is particularly susceptible to pattern center error, which is why real reference patterns are preferred when calculating gradients in the lattice distortion, such as when calculating geometrically necessary dislocation content (e.g., [33–37]), or looking at distributions of relative stress to infer information about the total dislocation content [38, 39]. A number of methods have been proposed to reduce pattern center error [14–17], but many are limited by degeneracy in determining pattern center and deformation [18, 19]. Another fundamental flaw in HREBSD methods is that strains in the lattice of a material are not strictly equivalent to strains in diffraction space. This is because band widths change with respect to Bragg's law, meaning that Equation 5 is only strictly true when $\mathbf{F}$ is a pure rotation. The assumption that deformation in real space is equal to the deformation of the diffraction pattern is reasonable because the effect of changing band widths is small compared to changes in the angle between bands. Lattice parameter information contained in the bandwidths can be extracted using band profile techniques [40, 41].

Another source of error is associated with the use of normalized cross-correlation to determine shifts

when the misorientation between the patterns is high. The computed values of $\vec{q}$ will be less accurate because cross-correlation does not take into account warping of the ROI, only the change in position. This may be addressed by remapping the pattern based on Equation 5 and some interpolation scheme of the pattern. Remapping methods allow the extension of 200 microstrain accuracy with up to an 11^{o} misorientation [10]. Typically, only one remap is done [10], but it can be performed iteratively for greater precision [20].

Three different versions of cross correlation HREBSD are implemented here for comparison with ICGN HREBSD, which will be explained in detail in the following section. The three cross-correlation methods are simple cross-correlation, cross-correlation with remapping, and cross-correlation with iterative remapping. Cross-correlation with iterative remapping was implemented here approximately consistent with Maurice, et al.[20]. One difference is that instead of Gaussian interpolation, a cubic B-spline was used to be consistent with the ICGN implementation. The spline coefficients must only be calculated once per reference pattern. This algorithm is presented in detail in Algorithm 1. The other two cross-correlation methods are not outlined for brevity.

```
1: Calculate spline coefficients for reference pattern
2: for i ≤ number of test patterns do
    3: Select an initial guess for F_old, such as from conventional EBSD indexing
    4: while ||ΔF − I|| > 10^−5 do
        5: Remap the relevant portion of the reference pattern according to F_old using the warp
           equation (Equation 12) and the reference pattern spline coefficients
        6: for j ≤ number of ROIs do
            7: Convolve the jth ROI on the remapped reference pattern and the test pattern via
               Fourier transforms while applying a band pass filter
            8: Calculate q by fitting the correlation peak
        end
        9: Compute ΔF from the values of q
        10: Update F_old = ΔF F_old
    end
end
```

Algorithm 1: Iterative pattern remapping HREBSD algorithm

3. Method

The core of HREBSD is inherently an optimization problem, i.e., determining a set of warping parameters that would deform the reference pattern to match the deformed pattern. The degree to which the

patterns match is referred to as the correlation criteria. For instance, normalized cross-correlation, which is used for conventional HREBSD, minimizes the dot product of the normalized ROIs (also referred to as the normalized cross-correlation criterion). The normalized least squares criterion has been shown to be functionally equivalent to the normalized cross-correlation criterion [42, 43], and because the normalized least squares criterion is more computationally tractable, it is used as the objective function for the method presented in this work.

This paper uses the ICGN method for DIC to minimize the objective function. ICGN is an iterative method that works by perturbing the reference ROI upon each iteration. The inverse of that perturbation is then added to the current best guess for the warp between the patterns. In the context of HREBSD this means the perturbation, $\Delta\mathbf{F}$, which is what the algorithm calculates each iteration, is inversely composed with respect to $\mathbf{F}$ from the previous iteration, $\mathbf{F}_{old}$, i.e.:

$$\mathbf{F}_{new} = \mathbf{F}_{old}\Delta\mathbf{F}^{-1} \tag{10}$$

The advantage of ICGN over other gradient-based methods is that the Hessian need only be estimated once, rather than calculated analytically at each step as in forward additive Gauss-Newton [25], or constantly updated numerically from some initial guess, as in generalized reduced gradient optimization. In a typical EBSD scan, each point in a grain is compared to a single reference pattern. This means that the Hessian actually only needs to be calculated once per grain.

The objective function is the normalized least squares criterion. Use of a normalized criterion accounts for the variation in local intensity of an image. In the case of an EBSD pattern, where the intensity drops off near the edges of the phosphor screen, normalization is particularly important. The normalized least squares criterion is formulated in the context of ICGN as follows:

$$C_{LS} = \sum_{i=1}^{N}\left[\frac{f^{(i)} - f_m}{\sqrt{\sum_{i=1}^{N}\left[f^{(i)} - f_m\right]^2}} - \frac{g^{(i)} - g_m}{\sqrt{\sum_{i=1}^{N}\left[g^{(i)} - g_m\right]^2}}\right]^2 \tag{11}$$

In this equation, $f^{(i)}$ and $g^{(i)}$ are short hand for the expressions $f(\vec{w}(\vec{x}^{(i)}, \Delta\mathbf{F}, \vec{P}, \vec{0}))$ and $g(\vec{w}(\vec{x}^{(i)}, \mathbf{F}_{old}, \vec{P}, \Delta\vec{P}))$, where functions $f(\vec{x})$ and $g(\vec{x})$ represent the greyscale value at a point $\vec{x}$ in the reference and test patterns, respectively. The set $\{\vec{x}^{(i)}...\vec{x}^{(N)}\}$ represents the points on the reference pattern that constitute an ROI and $\vec{w}(\vec{x}^{(i)}, \mathbf{F}, \vec{P}, \Delta\vec{P})$ represents the warp function based on Equation 5 (and substituting

in Equation 2):

$$\vec{w}(\vec{x}^{(i)},\mathbf{F},\vec{P},\Delta\vec{P}) = \vec{x}^{(i)} + \vec{q}^{(i)} = \Delta\vec{P} + \mathbf{F}(\vec{x}^{(i)} - \vec{P})\frac{-(\vec{P}+\Delta\vec{P})\cdot\hat{z}}{\mathbf{F}(\vec{x}^{(i)} - \vec{P})\cdot\hat{z}} + \vec{P} \tag{12}$$

This non-polynomial warping function is what differentiates ICGN HREBSD from other implementations of ICGN DIC. The expressions f_m and g_m are simply the mean pixel intensity values of the reference ROI and the test ROI:

$$f_m = \frac{\sum_{i=1}^{N} f^{(i)}}{N} \tag{13}$$

$$g_m = \frac{\sum_{i=1}^{N} g^{(i)}}{N} \tag{14}$$

Note that the patterns must be interpolated in order to calculate an intensity value at a non-integer point on the camera, $\vec{x}$. Here a bicubic B-spline is used for interpolation. Biquintic B-splines, which are used in some DIC algorithms, were also evaluated, but were not found to significantly improve results.

By approximating Equation 11 as quadratic with respect to $\mathbf{F}$, $\Delta\mathbf{F}$ may be calculated by solving the following equation:

$$\nabla\nabla C_{LS}\cdot\Delta\mathbf{F} = -\nabla C_{LS} \tag{15}$$

The following assumptions are made to estimate the gradient:

$$\frac{d}{d\Delta\mathbf{F}} f_m \approx 0 \tag{16}$$

$$\frac{d}{d\Delta\mathbf{F}} \sqrt{\sum_{i=1}^{N}\left[f^{(i)} - f_m\right]^2} \approx 0 \tag{17}$$

This gives the estimate of the gradient as:

$$\nabla C_{LS} = \left.\frac{dC_{LS}}{d\Delta\mathbf{F}}\right|_{\Delta\mathbf{F}=\mathbf{I}} \approx \frac{2}{\sqrt{\sum\left[f^{(i)} - f_m\right]^2}} \sum_{i=1}^{N}\left[\left[\frac{f^{(i)} - f_m}{\sqrt{\sum\left[f^{(i)} - f_m\right]^2}} - \frac{g^{(i)} - g_m}{\sqrt{\sum\left[g^{(i)} - g_m\right]^2}}\right]\left[\frac{df^{(i)}}{d\Delta\mathbf{F}}\right]\right]\Bigg|_{\Delta\mathbf{F}=\mathbf{I}} \tag{18}$$

To estimate the Hessian, the following Gauss-Newton assumption is made:

$$\sum\left[\frac{f^{(i)} - f_m}{\sqrt{\sum\left[f^{(i)} - f_m\right]^2}} - \frac{g(\vec{w}^{(i)} - g_m}{\sqrt{\sum\left[g^{(i)} - g_m\right]^2}}\right]\left[\frac{d^2 f^{(i)}}{d\Delta\mathbf{F}^2}\right] \approx 0 \tag{19}$$

With this assumption, the estimate for the Hessian becomes:

$$\nabla\nabla C_{LS} = \left.\frac{d^2 C_{LS}}{d\Delta\mathbf{F}^2}\right|_{\Delta\mathbf{F}=\mathbf{I}} \approx \frac{2}{\sqrt{\sum\left[f^{(i)} - f_m\right]^2}} \left[\frac{df^{(i)}}{d\Delta\mathbf{F}}\right] \otimes \left[\frac{df^{(i)}}{d\Delta\mathbf{F}}\right]\Bigg|_{\Delta\mathbf{F}=\mathbf{I}} \tag{20}$$

The Hessian is factored using Cholesky decomposition for more efficiency. For each iteration, the gradient is calculated, Equation 15 is solved for $\Delta\mathbf{F}$, and then $\mathbf{F}$ is updated according to Equation 10. The algorithm then iterates until the norm of $\Delta\mathbf{F}$ falls under a pre-defined threshold; in this paper the threshold for convergence was set to 10 microstrain. Iterating further did not improve accuracy on a simulated data set..

In order to calculate the Hessian and gradient, it is first necessary to calculate the derivative of $f^{(i)}$ with respect to $\Delta\mathbf{F}$, $\frac{d}{d\Delta\mathbf{F}} f^{(i)}$. This gradient is calculated as follows:

$$\frac{df^{(i)}}{d\Delta\mathbf{F}} = \frac{\partial f^{(i)}}{\partial w_1}\frac{dw_1}{d\Delta\mathbf{F}} + \frac{\partial f^{(i)}}{\partial w_2}\frac{dw_2}{d\Delta\mathbf{F}} \tag{21}$$

where $\vec{w} = \vec{w}(\vec{x}^{(i)}, \Delta\mathbf{F}, \vec{P}, \vec{0})$. In this equation $\frac{\partial}{\partial w_1} f^{(i)}$ and $\frac{\partial}{\partial w_2} f^{(i)}$ are calculated using the spline fit, and will be abbreviated as f_1 and f_2, respectively. The gradient is expanded component-wise in Equations 22-30:

$$\frac{df^{(i)}}{d\Delta F_{11}} = f_1(x_1 - P_1) \tag{22}$$

$$\frac{df^{(i)}}{d\Delta F_{12}} = f_1(x_2 - P_2) \tag{23}$$

$$\frac{df^{(i)}}{d\Delta F_{13}} = -P_3 f_1 \tag{24}$$

$$\frac{df^{(i)}}{d\Delta F_{21}} = f_2(x_1 - P_1) \tag{25}$$

$$\frac{df^{(i)}}{d\Delta F_{22}} = f_2(x_2 - P_2) \tag{26}$$

$$\frac{df^{(i)}}{d\Delta F_{23}} = -P_3 f_2 \tag{27}$$

$$\frac{df^{(i)}}{d\Delta F_{31}} = [f_1(x_1 - P_1) + f_2(x_2 - P_2)]\frac{x_1 - P_1}{P_3} \tag{28}$$

$$\frac{df^{(i)}}{d\Delta F_{32}} = [f_1(x_1 - P_1) + f_2(x_2 - P_2)]\frac{x_2 - P_2}{P_3} \tag{29}$$

$$\frac{df^{(i)}}{d\Delta F_{33}} = -f_1(x_1 - P_1) - f_2(x_2 - P_2) \tag{30}$$

The first six terms of the gradient of $f^{(i)}$ with respect to $\Delta\mathbf{F}$ (Equations 22-27) are identical to the gradient if the warping function were a simple linear deformation. Equations 28-29 account for the non-linearity of the warping function caused by the projection of the pattern onto a 2D surface. Equation 30 is a linear combination of Equation 22 and Equation 26, meaning that the Hessian will be rank deficient, just as not all nine degrees of freedom are available from cross-correlation HREBSD. To overcome this issue, only the deviatoric component of the strain is recovered.

One advantage of this method is that it only requires a single ROI per pattern instead of a large number of smaller, overlapping ROIs, making computation much more efficient. The same principle that suggests that the ideal arrangement of ROIs for cross-correlation HREBSD is annular implies that the ideal ROI shape for ICGN HREBSD is an annulus. This ROI is a completely arbitrary shape, and could be adapted to maximize the area compared between patterns [20, 24]. An adaptive ROI, however, precludes precomputation of the Hessian for each grain. Also, pattern area near the edges has lower intensity and is more highly distorted, which leads to spline fit error. All these factors must be taken into account when selecting an ROI shape and size.

Note that the method described here, ICGN HREBSD, is actually very similar to cross-correlation HREBSD with remapping. Both may be thought of as optimization methods that seek a set of warping parameters that maximize correlation between two patterns. The differences lie in the means by which the step is determined. The algorithm for ICGN HREBSD is outlined in Algorithm 2. There are a number of similarities with the remapping algorithm shown in Algorithm 1.

4. Results

The performance of ICGN HREBSD was evaluated with the use of simulated EBSD patterns produced with EMsoft [44]. EMsoft is an open-source software package capable of simulating EBSD patterns using a combination of dynamical scattering (for the diffraction bands) and Monte Carlo simulation (for the intensity background). Simulated patterns are convienient for the evaluation of HREBSD techniques, because

1: Calculate spline coefficients for reference pattern
2: Compute $\frac{df^{(i)}}{d\Delta\mathbf{F}}$ for each point in the reference ROI (Equations 22-30)
3: Compute and perform Cholesky decomposition on the Hessian estimate (Equation 20)
4: **for** $i \leq$ *number of test patterns* **do**
    5: Calculate spline coefficients for current test pattern
    6: Select an initial guess for $\mathbf{F}_{old}$, such as from conventional EBSD indexing
    7: **while** $||\Delta\mathbf{F} - \mathbf{I}|| > 10^{-5}$ **do**
        8: Calculate $g^{(i)}$ using the warp equation (Equation 12) and the test pattern spline coefficients
        9: Calculate the ∇C_{LS} (Equation 18)
        10: Calculate $\Delta\mathbf{F}$ (Equation 15)
        11: Update $\mathbf{F_{old}}$ (Equation 10)
    end
end

Algorithm 2: ICGN HREBSD algorithm

comparison of measured values to simulated values provides an estimate of the error [10, 24, 45]. Several instances of cross-correlation HREBSD were also implemented: simple cross-correlation, cross-correlation with remapping, and cross-correlation with iterative remapping. The simulated material was aluminum. The reference orientation was aligned with the sample. The simulated sample tilt and camera elevation are 70^{o} and 10^{o} respectively. Test patterns were taken by rotating about the $[111]$ crystallographic axis from 0^{o} to 12^{o}, stepping in increments of 0.3^{o}. After 12^{o} there are too few features common to both patterns for proper comparison. While each method may be adapted to overcome this difficulty, these adaptations are difficult to standardize between ICGN and cross-correlation HREBSD, making comparison difficult. The simulated patterns were 960×960 pixels. The patterns were saved with an 8 bit depth spanning the maximum and minimum intensity. Because of the intensity of a zone axis, only about half of the bit depth was effectively utilized. EMsoft employs Monte Carlo simulations to simulate the drop off in intensity that occurs farther from the pattern center. The pattern center for each pattern was the same: $\vec{P} = [.5; .5; .625]$, in units of fraction of the phosphor screen width. An example pattern is shown in Figure 2.

The ROI for the ICGN method was the set of pixels fully enclosed by an annulus centered about the center of the diffraction pattern with an outer radius of 35.5% of the phosphor screen size, and a thickness of 15% of the phosphor screen size. One hundred partially overlapping ROIs were used for the cross-correlation methods. They were arranged annularly about the center of the diffraction image, with their centers 29.4% from the center of the pattern, and the ROI width 15% of the phosphor size. These parameters

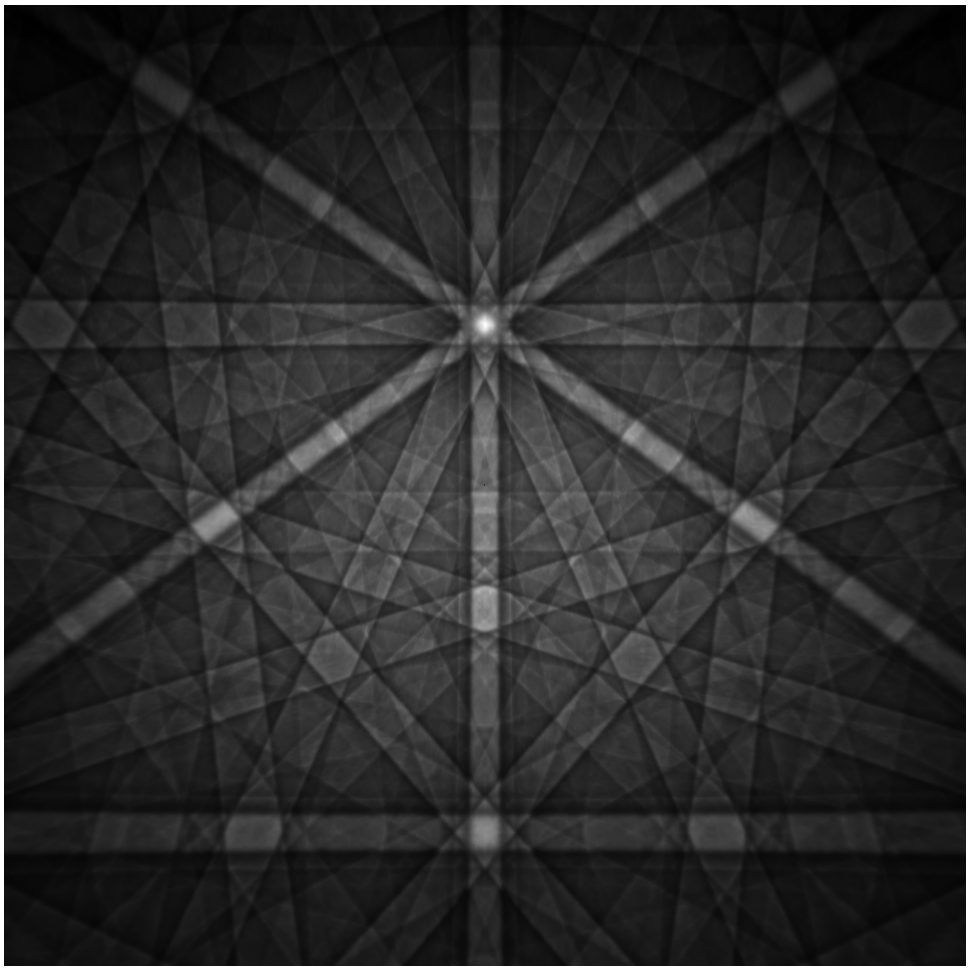

Figure 2: One of the aluminum EBSD patterns simulated with EMsoft.

were selected such that both methods performed optimally on the pattern misoriented 6^{o} from the reference. Sensitivity to these parameters varies between the methods primarily because cross-correlation HREBSD does not weight each point equally due to ROI overlap. Cross-correlation HREBSD was optimized when the outer radius of the ROIs was maximized, and this parameter was constrained by the amount of rotation required. In contrast, the ICGN method acheived optimal performance when the ROI had an intermediate outer radius, possibly due to the balance between sensitivity of deformation to the distance from the pattern center and the noise due to imperfect interpolation. The initial guess for the orientation of each test pattern was perturbed on a random axis by 0.1^{o}. Increasing or decreasing this expected error only affected the number of iterations till convergence, not the optimal solution. Once the error was increased to over a degree, convergence was much less likely, and it became necessary to use conventional cross-correlation as

the initial guess.

The misorientation between the correct solution and the measured solution for each method is shown in Figure 3. The cross-correlation method has a dramatic decrease in accuracy with increasing misorientation, which was the primary motivation for the original development of the remapping [10, 20]. The remapping method is able to maintain a much higher level of accuracy than the cross-correlation method. Figure 3 also illustrates that error for the iterative remapping method is always lower than its non-iterating counterpart. Thus, the addition of an iterative scheme improves the accuracy of the standard remapping method. The mean misorientation error for the 40 simulated patterns is 0.00530° for the ICGN compared to the 0.00544° for iterative remapping, indicating a very small edge in accuracy for ICGN.

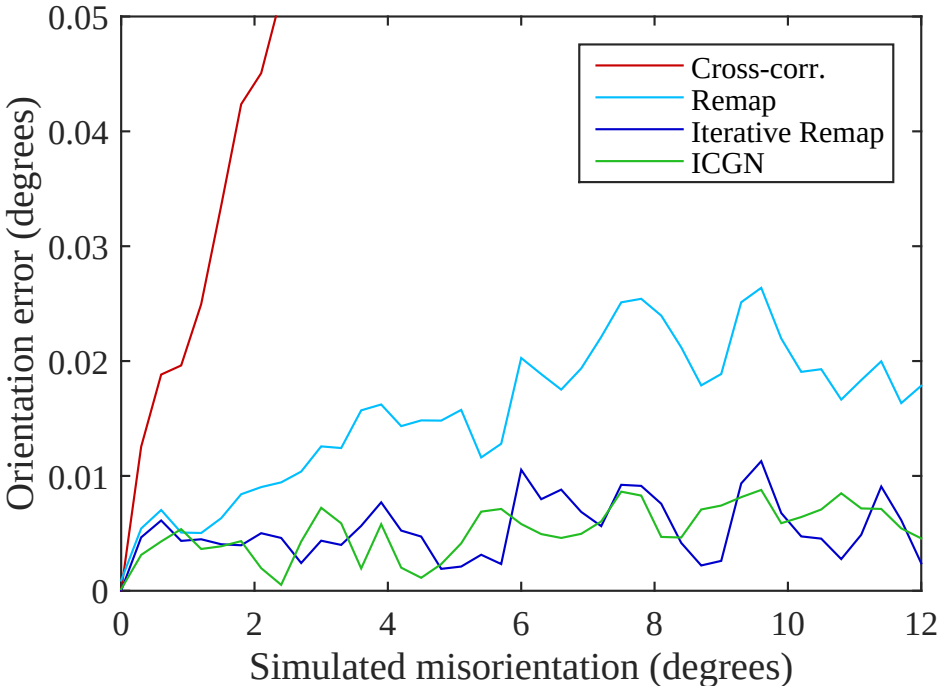

Figure 3: Misorientation between each HREBSD method's measured rotation and the simulated rotation.

Because the strain portion of the deformation is often of interest, the 2-norm of the strain (as separated via polar decomposition) for each method is shown in Figure 4. The simulated strain is zero in all cases, so the norm of this strain represents an estimate of the strain resolution of the methods. The trend here is similar to Figure 3 in that iterative remapping is more accurate than simple remapping which is more accurate than cross-correlation. Notably, the ICGN method now significantly outperforms even the iterative

remapping scheme. The ICGN method has a mean strain error on this test of 78 microstrain compared to 397 and 198 for simple remapping and iterative remapping, respectively. This represents 80% and 60% reduction of error by using the ICGN method. The ICGN method is able to keep strain error below the 200 microstrain threshold for all cases (up to 12°), whereas the remapping method is only able to maintain this threshold through 2° and 6° for iterative remapping.

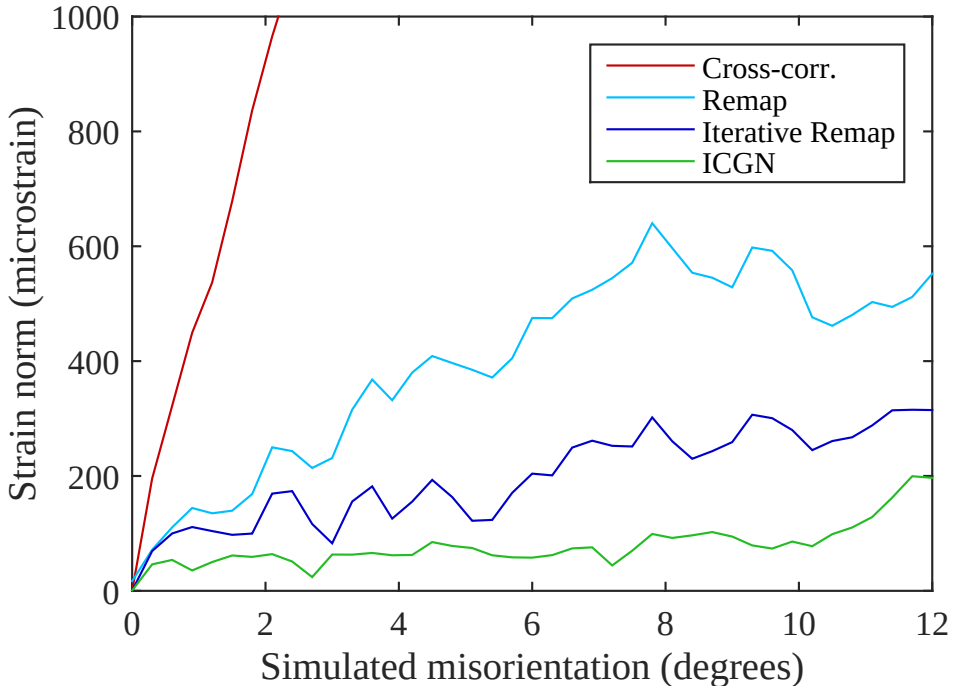

Figure 4: Norm of the erroneous strain measured by each method.

The difference between the simulated deformation and the deformation measured via ICGN HREBSD is expressed component-wise in Figure 5(a). The component-wise error for the iterative remapping is shown in 5(b). The result for the two methods is similar save for one exception: cross-correlation with remapping has more noise in the F_{31} and F_{32} components, the terms associated with non-linear deformation (marked with dashed lines in Figure 5). These two components of the error (and thus the strain error) have a lower magnitude for the ICGN method, presumably because ICGN explicitly accounts for this non-linearity.

Overall, the other three methods clearly outperform conventional cross-correlation HREBSD after the first 0.3°. Note that in terms of relative error, the conventional cross-correlation method was only off by an average of 2%. Single iteration remapping performed worse than either of the iterative methods, as expected,

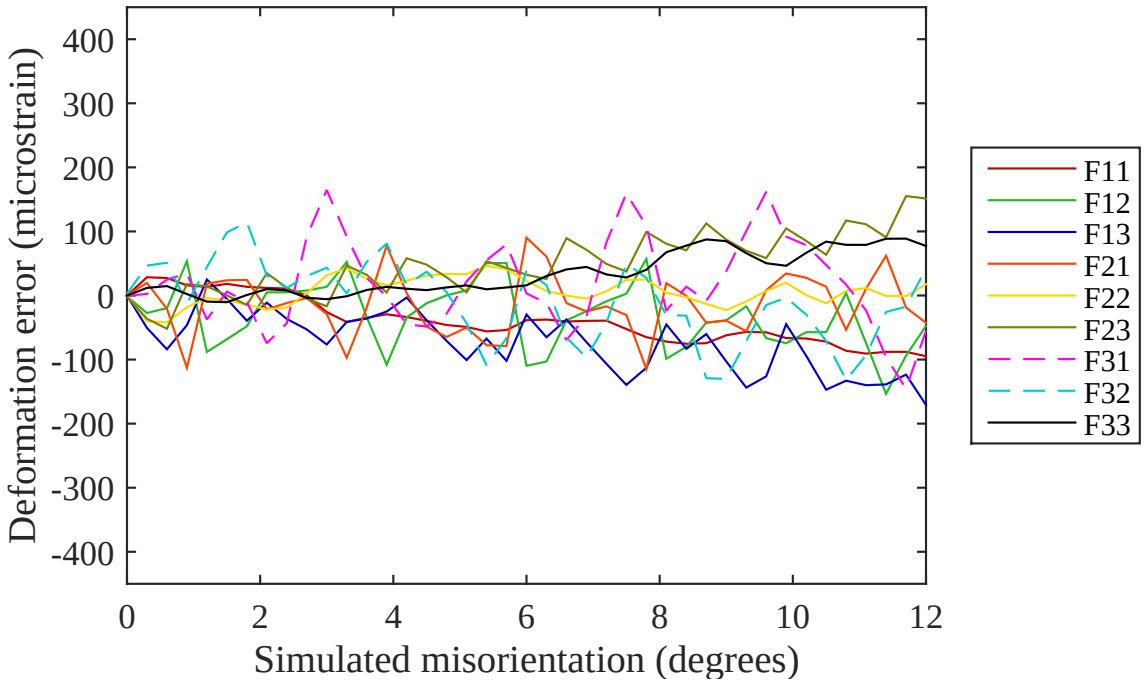

(a)

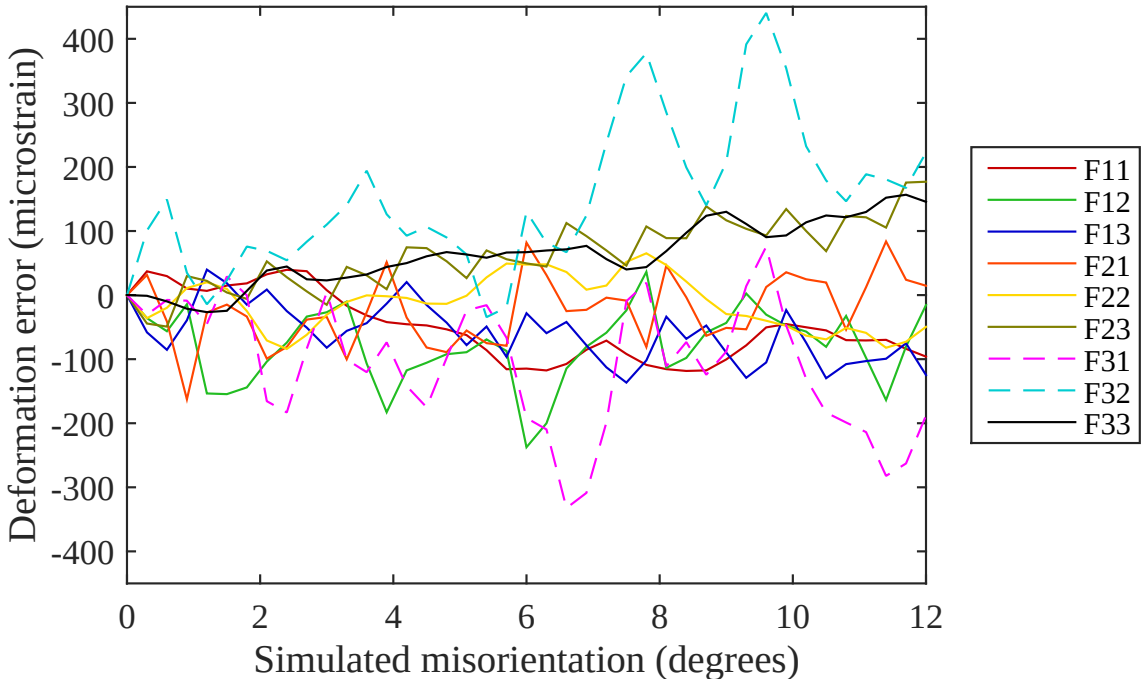

(b)

Figure 5: Components of the deviation between the simulated rotation and the measured distortion for the (a) ICGN method and the (b) iterative remapping method.

although this depends largely on the accuracy of the initial guess. ICGN had comparable orientation error to iterative remapping, but significantly better strain resolution. Care must be taken when comparing the error levels presented here with what is reported for remapping [10] and a similar DIC-based approach [24] because of substantial differences in the simulated data sets, i.e. utilization of bit depth, pixel density, material selection and, perhaps most importantly, the inclusion of a realistic intensity background.

The increased accuracy of the methods using pattern interpolation came at a significant computational price. Simple remapping took 5 times longer than standard cross-correlation HREBSD, iterative remapping took 15 times longer, and ICGN took about 12 times longer. Iterative remapping and ICGN both took 3-4 iterations to converge. The most computationally expensive step was the remapping itself (step 8 in Algorithm 2 and step 5 in Algorithm 1). Since this step is identical between the two methods when remapping the same area of the patterns, the computation times per iteration are very similar. However, the code used has yet to be optimized or even adapted for parallel computing, so these computation times are only intended to estimate the computational expense of each algorithm.

5. Conclusion

This work presents ICGN HREBSD, a new method of HREBSD adapted from ICGN DIC that accounts for the distortion of a pattern based on projection parameters in the warping function. This method is analogous to conventional cross-correlation techniques with remapping. Tests were performed on simulated patterns over a range of 12 degrees of misorientation using the ICGN method, conventional cross-correlation, cross-correlation with remapping and cross-correlation with iterative remapping. The ICGN method was shown to have about half of the strain error of iterative remapping, for comparable computation time, and about a quarter of the strain error of single iteration remapping. This improvement in accuracy probably stems from addressing the shift and deformation of the pattern in a single step. The strain resolution of this technique will vary based on the bit depth and resolution of the pattern, the pattern center, the detector distance, and the noise that exists in real patterns. Improvements in HREBSD characterization techniques like those presented in this work will allow their direct incorporation into calibration and development of high fidelity material models.

References

[1] F. Ram, S. Zaefferer, T. Jäpel, D. Raabe, Error analysis of the crystal orientations and disorientations obtained by the classical electron backscatter diffraction technique, Journal of Applied Crystallography 48 (3) (2015) 797–813.

[2] S. Wright, M. Nowell, J. Basinger, Precision of EBSD based orientaion measurements, Microscopy and Microanalysis 17 (2011) 406–407.

[3] S. I. Wright, M. M. Nowell, R. de Kloe, L. Chan, Orientation precision of electron backscatter diffraction measurements near grain boundaries, Microscopy and Microanalysis 20 (2014) 852–863.

[4] C. Sorensen, J. A. Basinger, M. M. Nowell, D. T. Fullwood, Five-parameter grain boundary inclination recovery with EBSD and interaction volume models, Metallurgical and Materials Transactions A 45 (9) (2014) 4165–4172.

[5] H. Lim, S. Subedi, D. Fullwood, B. Adams, R. Wagoner, A practical meso-scale polycrystal model to predict dislocation densities and the Hall-Petch effect, Materials Transactions 55 (1) (2014) 35–38.

[6] T. Zhang, D. M. Collins, F. P. Dunne, B. A. Shollock, Crystal plasticity and high-resolution electron backscatter diffraction analysis of full-field polycrystal Ni superalloy strains and rotations under thermal loading, Acta Materialia 80 (0) (2014) 25 – 38.

[7] K. Troost, P. van der Sluis, D. Gravesteijn, Microscale elastic-strain determination by backscatter Kikuchi diffraction in the scanning electron microscope, Appl. Phys. Lett. 62 (10) (1993) 1110–1112.

[8] A. J. Wilkinson, G. Meaden, D. J. Dingley, High resolution mapping of strains and rotations using electron back scatter diffraction, Materials Science and Technology 22 (11) (2006) 1–11.

[9] A. J. Wilkinson, G. Meaden, D. J. Dingley, High-resolution elastic strain measurement from electron backscatter diffraction patterns: New levels of sensitivity, Ultramicroscopy 106 (2006) 307–313.

[10] T. Britton, A. Wilkinson, High resolution electron backscatter diffraction measurements of elastic strain variations in the presence of larger rotations, Ultramicroscopy 114 (2012) 82–95.

[11] J. Jiang, T. Britton, A. Wilkinson, Measurement of geometrically necessary dislocation density with high resolution electron backscatter diffraction: Effects of detector binning and step size, Ultramicroscopy 125 (2013) 1–9.

[12] L. T. Hansen, B. E. Jackson, D. T. Fullwood, S. I. Wright, M. De Graef, E. R. Homer, R. H. Wagoner, Influence of noise-generating factors on cross-correlation electron backscatter diffraction (EBSD) measurement of geometrically necessary dislocations (GNDs), Microscopy and Microanalysis 23 (3) (2017) 460–471.

[13] T. J. Ruggles, G. F. Bomarito, A. H. Cannon, J. D. Hochhalter, Selectively electron-transparent microstamping toward concurrent digital image correlation and high-angular resolution electron backscatter diffraction (EBSD) analysis, Microscopy and Microanalysis 23 (6) (2017) 1091 – 1095.

[14] T. Britton, C. Maurice, R. Fortunier, J. Driver, A. Day, G. Meaden, D. Dingley, K. Mingard, A. Wilkinson, Factors affecting the accuracy of high resolution electron backscatter diffraction when using simulated patterns, Ultramicroscopy 110 (2010) 1443–1453.

[15] J. Basinger, D. Fullwood, J. Kacher, B. Adams, Pattern center determination in EBSD microscopy, Microscopy and Micro-

analysis 17 (2011) 330–340.

[16] K. Mingard, A. Day, C. Maurice, P. Quested, Towards high accuracy calibration of electron backscatter diffraction systems, Ultramicroscopy 111 (2011) 320–329.

[17] C. Maurice, D. Krzysztof, R. Fortunier, A method for accurate localisation of EBSD pattern centres, Ultramicroscopy 111 (2011) 140–148.

[18] J. Alkorta, Limits of simulation based high resolution EBSD, Ultramicroscopy 131 (2013) 33–38.

[19] J. Alkorta, M. Marteleur, P. J. Jacques, Improved simulation based HR-EBSD procedure using image gradient based DIC techniques, Ultramicroscopy 182 (2017) 17 – 27.

[20] C. Maurice, J. H. Driver, R. Fortunier, On solving the orientation gradient dependency of high angular resolution EBSD, Ultramicroscopy 113 (2012) 171–181.

[21] H. Schreier, J.-J. Orteu, M. A. Sutton, Image correlation for shape, motion and deformation measurements, Springer US, 2009.

[22] B. Pan, K. Qian, H. Xie, A. Asundi, Two-dimensional digital image correlation for in-plane displacement and strain measurement: a review, Measurement science and technology 20 (6) (2009) 062001.

[23] J. Blaber, B. Adair, A. Antoniou, Ncorr: open-source 2d digital image correlation matlab software, Experimental Mechanics 55 (6) (2015) 1105–1122.

[24] T. Vermeij, J. Hoefnagels, A consistent full-field integrated dic framework for HR-EBSD, Ultramicroscopy-doi:https://doi.org/10.1016/j.ultramic.2018.05.001.
URL http://www.sciencedirect.com/science/article/pii/S0304399117305363

[25] S. Baker, I. Matthews, Lucas-Kanade 20 years on: A unifying framework, International Journal of Computer Vision 56 (3) (2004) 221–255.

[26] B. Pan, K. Li, W. Tong, Fast, robust and accurate digital image correlation calculation without redundant computations, Experimental Mechanics 53 (7) (2013) 1277–1289.

[27] J. P. Lewis, Fast normalized cross-correlation, in: Vision interface, Vol. 10, 1995, pp. 120–123.

[28] T. Hardin, T. Ruggles, D. Koch, S. Niezgoda, D. Fullwood, E. Homer, Analysis of traction-free assumption in high-resolution EBSD measurements, Journal of Microscopy.

[29] T. Britton, J. Jiang, R. Clough, E. Tarleton, A. Kirkland, A. Wilkinson, Assessing the precision of strain measurements using electron backscatter diffraction part 2: Experimental demonstration, Ultramicroscopy 135 (2013) 136 – 141.

[30] J. Kacher, C. Landon, B. L. Adams, D. Fullwood, Braggs law diffraction simulations for electron backscatter diffraction analysis, Ultramicroscopy 109 (9) (2009) 1148–1156.

[31] D. Fullwood, M. Vaudin, C. Daniels, T. Ruggles, S. I. Wright, Validation of kinematically simulated pattern HR-EBSD for measuring absolute strains and lattice tetragonality, Materials Characterization 107 (2015) 270 – 277.

[32] B. E. Jackson, J. J. Christensen, S. Singh, M. De Graef, D. T. Fullwood, E. R. Homer, R. H. Wagoner, Performance of dynamically simulated reference patterns for cross-correlation electron backscatter diffraction, Microscopy and Microanalysis 22 (4) (2016) 789–802.

[33] T. J. Ruggles, D. T. Fullwood, Estimations of bulk geometrically necessary dislocation density using high resolution EBSD, Ultramicroscopy 133 (2013) 8–15.

[34] T. Ruggles, D. Fullwood, J. Kysar, Resolving geometrically necessary dislocation density onto individual dislocation types using EBSD-based continuum dislocation microscopy, International Journal of Plasticity 76 (2016) 231 – 243.

[35] T. Ruggles, T. Rampton, A. Khosravani, D. Fullwood, The effect of length scale on the determination of geometrically necessary dislocations via EBSD continuum dislocation microscopy, Ultramicroscopy 164 (2016) 1 – 10.

[36] S. R. Yeratapally, J. D. Hochhalter, T. J. Ruggles, M. D. Sangid, Investigation of fatigue crack incubation and growth in cast MAR-M247 subjected to low cycle fatigue at room temperature, International Journal of Fracture (2017) 1–18.

[37] B. E. Dunlap, T. J. Ruggles, D. T. Fullwood, B. Jackson, M. A. Crimp, Comparison of dislocation characterization by electron channeling contrast imaging and cross-correlation electron backscattered diffraction, Ultramicroscopy 184 (2018) 125 – 133.

[38] A. J. Wilkinson, E. Tarleton, A. Vilalta-Clemente, J. Jiang, T. B. Britton, D. M. Collins, Measurement of probability distributions for internal stresses in dislocated crystals, Applied Physics Letters 105 (18) (2014) –.

[39] S. Kalácska, I. Groma, A. Borbély, P. D. Ispánovity, Comparison of the dislocation density obtained by HR-EBSD and X-ray profile analysis, Applied Physics Letters 110 (9) (2017) 091912.

[40] I. Fodchuk, S. Balovsyak, M. Borcha, Y. Garabazhiv, V. Tkach, Determination of structural homogeneity of synthetic diamonds from analysis of kikuchi lines intensity distribution, Semiconductor Physics Quantum Electronics & Optoelectronics.

[41] F. Ram, S. Zaefferer, D. Raabe, Kikuchi bandlet method for the accurate deconvolution and localization of Kikuchi bands in Kikuchi diffraction patterns, Journal of Applied Crystallography 47 (2014) 264–275.

[42] W. Tong, An evaluation of digital image correlation criteria for strain mapping applications, Strain 41 (4) (2005) 167–175.

[43] B. Pan, H. Xie, Z. Wang, Equivalence of digital image correlation criteria for pattern matching, Applied optics 49 (28) (2010) 5501–5509.

[44] S. Singh, F. Ram, M. De Graef, EMsoft: Open source software for electron diffraction/image simulations, Microscopy and Microanalysis 23 (S1) (2017) 212 – 213.

[45] S. Villert, C. Maurice, C. Wyon, R. Fortunier, Accuracy assessment of elastic strain measurement by EBSD, Journal of Microscopy 233 (2) (2009) 290301.